

Estimation of Orientation and Camera Parameters from Cryo-Electron Microscopy Images with Variational Autoencoders and Generative Adversarial Networks

Nina Miolane
Stanford University
nmiolane@stanford.edu

Frédéric Poitevin
Stanford University
frederic.poitevin@stanford.edu

Yee-Ting Li
SLAC National Accelerator
ytl@slac.stanford.edu

Susan Holmes
Stanford University
susan@stat.stanford.edu

Abstract

Cryo-electron microscopy (cryo-EM) is capable of producing reconstructed 3D images of biomolecules at near-atomic resolution. As such, it represents one of the most promising imaging techniques in structural biology. However, raw cryo-EM images are only highly corrupted - noisy and band-pass filtered - 2D projections of the target 3D biomolecules. Reconstructing the 3D molecular shape starts with the removal of image outliers, the estimation of the orientation of the biomolecule that has produced the given 2D image, and the estimation of camera parameters to correct for intensity defects. Current techniques performing these tasks are often computationally expensive, while the dataset sizes keep growing. There is a need for next-generation algorithms that preserve accuracy while improving speed and scalability. In this paper, we combine variational autoencoders (VAEs) and generative adversarial networks (GANs) to learn a low-dimensional latent representation of cryo-EM images. We perform an exploratory analysis of the obtained latent space, that is shown to have a structure of “orbits”, in the sense of Lie group theory, consistent with the acquisition procedure of cryo-EM images. This analysis leads us to design an estimation method for orientation and camera parameters of single-particle cryo-EM images, together with an outliers detection procedure. As such, it opens the door to geometric approaches for unsupervised estimations of orientations and camera parameters, making possible fast cryo-EM biomolecule reconstruction.

1. Introduction

Cryo-electron microscopy (cryo-EM) is one of the most promising imaging techniques in biology, as it produces 3D reconstructions of biomolecules at near-atomic resolution. However, raw cryo-EM images are only highly corrupted 2D projections of the target 3D biomolecules. The required reconstruction of the 3D molecular shape starts with the removal of image outliers, the estimation of the biomolecule’s 3D orientation that has produced each 2D image, and the estimation of camera parameters at acquisition. This paper proposes a neural network architecture with geometric regularization in order to perform these three tasks in the latent space of a variational autoencoder.

1.1. Cryo-EM images acquisition and preprocessing

Over the years, protocols for cryo-EM data collection and data processing have matured into a well-defined pipeline [36, 16, 49]. The biomolecule of interest is prepared in an aqueous solution. The solution is deposited on a grid, flash-frozen to cryogenic temperature, and inserted in the vacuum chamber of an electron microscope, where it scatters an incoming electron beam. The resulting beam goes through complex optical systems and hits a detector where it generates magnified images of a region of interest (ROI) of the grid: a micrograph. Modern detectors can collect micrographs at increasing reading rate and sensitivity, thus allowing them to collect thousands of dose-fractionated micrograph movies per data collection campaign [35]. Each micrograph movie can then be averaged into a micrograph image with better signal-to-noise ratio while compensating for in-plane translational drift that might occur between frames [53]. A combination of these improvements in hardware and software solutions have been key in the “resolution revolution” of cryo-EM [30].

The imaging process convolves the “true” image with the point-spread-function (PSF) of the microscope, thereby effectively band-pass filtering it. The parameters of the PSF are evaluated by fitting its Fourier transform, the contrast-transfer-function (CTF), to the Fourier transform of each micrograph [40, 52]. A key parameter of the CTF function is the defocus: the distance between the image plane and the detector plane. Typical experiments collect over a uniform range of defocus, typically [0.5 μm , 2.5 μm], in order to cover all spatial frequencies uniformly.

The ROI imaged is typically made of a solvent region embedding multiple copies of the biomolecule studied. At variance with cryo-electron tomography *in-situ* [34] where geographical context matters, in single-particle imaging experiments [13] the dataset can be reduced to “particles” containing the molecule of interest extracted, or “picked”, from the micrograph (typically dozens to a few hundred particles per micrograph). Contamination of the sample and corruption of the images make this step highly error-prone. Theoretically, true positive particles correspond to images of the object that are informative for the reconstruction of its 3D volume. While manual picking is still possible, semi-automated (*e.g.* template-matching approaches [45]) and fully automated (*e.g.* reference-free picking through image filtering followed by a threshold-based segmentation step [56]) particle picking tools have been developed. However, their recall and precision vary, and it is still customary to filter out false positives afterward.

Filtering false positives is usually carried out at the so-called 2D classification step, where the dataset is clustered into a user-defined number of 2D classes. Ideally, classes separate false positive from true positive images and further separate the latter in groups of similar viewing angles [47]. Thus, 2D classification fulfills a data curating task while also optimizing the in-plane orientation and centering of true positive images. The underlying model used is a gaussian-mixture that is solved through an expectation-maximization (EM) algorithm. The algorithm iteratively assigns images to their respective class - through direct comparison with the current class reference, after optimization of in-plane rotation and translation, and then estimates the class parameters (class average and variance) [46, 44]. The user then discards or keeps classes, and retains the corresponding images for 3D reconstruction and further analysis.

1.2. Cryo-EM 3D reconstruction

1.2.1 Generative model and 3D reconstruction

At that stage, we assume the following image formation model under the weak phase approximation [17]:

$$x_i = \text{PSF}_i * P[R_i \cdot V] + \eta_i, \quad i = 1, \dots, n, \quad (1)$$

where x_i is a $p \times p$ particle image, V is a 3D grid of $p \times p \times p$ voxels whose projection is convolved with the PSF, and η is

the remaining part of the signal, typically assumed to be uncorrelated noise. The operator P projects the 3D volume along the Z-axis, after the reference volume V has been subjected to rotation R_i . We refer to R_i as the “orientation” of the particle. In general, the PSF is inherited from the micrograph from which the particle image was extracted, although it can also be further refined *a posteriori* [21, 56]. We refer to the PSF_i as the “camera parameters” that have generated the particle. We see that reconstructing V from the particle dataset amounts to estimating the rotation assuming they are all properly centered, and the PSF.

In Fourier space, summing over the Fourier coefficients indexed by l of an image x_i , for a given orientation R of V , a given PSF, and an expected noise η , we define the image alignment error E and its associated likelihood $E_i(R) = \frac{1}{2} \sum_l \frac{|\text{CTF}_l \cdot \tilde{P}_l[R \cdot V] - \tilde{x}_{il}|^2}{\sigma_l^2}$ and $\mathbb{P}(x_i | R, \mathbf{V}) \propto \exp -E_i(R)$. The reconstruction problem of inverting Equation 1 can be cast as a regularized least-square optimization problem [2]:

$$\text{argmin}_{V, \{R, \text{PSF}\}} f(V) = \sum_i E_i + H_{\text{prior}}. \quad (2)$$

Equivalently, this could be cast in a Bayesian formulation where we wish to find the best model Θ for our dataset, given unobserved variables $\phi = (R, \text{PSF})$ [43]. The model is a set that contains the function V and possibly other quantities, and the unobserved variables are the parameters of the operator P . The *maximum a posteriori* (MAP) estimate of the model Θ is found to optimize the posterior distribution $\mathbb{P}(\Theta | x, y)$, given the data x and the prior information y . Given the current model and the prior information, we note the *likelihood* of observing the data $\mathbb{P}(x | \Theta, y)$ and the *prior* is the likelihood of the current model given the prior information $\mathbb{P}(\Theta | y)$. According to Bayes’ law, the former factorizes into the latter: $\mathbb{P}(\Theta | x, y) \propto \mathbb{P}(x | \Theta, y) \mathbb{P}(\Theta | y)$, where the likelihood is marginalized over the unobserved variables ϕ : $\mathbb{P}(x | \Theta, y) = \int d\phi \mathbb{P}(x | \phi, \Theta) \mathbb{P}(\phi | y)$. To recapitulate, we want to maximize the posterior distribution:

$$\text{argmax}_{\Theta} f(\Theta) = \log \mathbb{P}(x | \Theta, y) + \log \mathbb{P}(\Theta | y). \quad (3)$$

Solving Equation 3 can be done in two steps: a reference-free *ab initio* reconstruction step that can be refined in a second step. We discuss them in the next section.

1.2.2 Computational cost

The authors of [38] proposed to perform fast identification of one or several low-resolution solutions (x that do not extend at high frequency in the Fourier domain) to Equation 3 using a stochastic gradient descent (SGD) optimization scheme [10]. Rather than computing the contribution of all images to Equation 3, SGD selects a random subset of

images at each optimization iteration and updates the estimate of V based on the gradient of the objective at that iteration. Each iteration becomes inexpensive, and the overall process insensitive to local optima, thereby yielding quickly a solution that approaches the global optima.

This solution can then be used to initialize the following refinement protocol that aims at finding a solution with the highest resolution possible. Such a protocol is described in [43], where Equation 3 is optimized by expectation maximization [14]. It iteratively refines the estimate of V , its power spectrum, and the power spectrum of the noise, that depend on the posterior probability of the orientation of each image, given the estimate of V at the previous step. This posterior probability is calculated numerically by systematically evaluating the agreement between each image and all possible orientation of the current model, at each iteration. This costly step has greatly benefited from parallelization using GPUs and hybrid clusters [26] or the implementation of a branch-and-bound algorithm [38] that rules out large regions of the search space, but it remains a computational bottleneck.

1.3. Related work

1.3.1 Deep learning advances

Deep learning techniques have started to penetrate the data processing pipeline, to speed-up the steps described in the previous subsection [5]. Researchers have trained neural networks to perform fast automated particle picking [51, 55, 50, 6, 7], particle pruning [42], as well as validation and estimation of the resolution of cryo-EM 3D reconstructions [4]. These advances have targeted and accelerated steps before or after the 3D reconstruction itself. They have not addressed the computational burden of the joint orientation estimations and volume reconstruction.

Recently, [54] used a spatial variational autoencoder (VAE) [7] to capture the heterogeneity of 3D structures within a continuous latent space. However, the architecture keeps a computational bottleneck in the orientation estimation required for volume reconstruction. The orientation R is not estimated through the VAE, but with a global search using a branch and bound algorithm, similar to [38]. In contrast, this paper specifically targets the orientation estimation using a VAE architecture.

1.3.2 Disentanglement of latent variables

Estimating the orientation implies being able to disentangle it from other variables in the latent space of a VAE. State-of-the-art methods for disentangling variables often rely on modifying the VAE loss function. The β -VAE heavily penalizes the regularization factor in the VAE loss and achieves good disentanglement results on images [48]. However, it is unclear if this penalization works for all

datasets. Other solutions choose to maximize the mutual information between a few latent variables and the observation (InfoGAN, [12]), an approximation of the total correlation (TC) (β -TCVAE, [11]), or the Hilbert-Schmidt Independence Criterion (dHSIC) [32] to enforce independence between the latent representations and arbitrary nuisance factors. Similarly, the variational fair autoencoder (VFAE) [33] uses priors that encourage independence between sensitive and latent factors of variation, to learn invariant representation.

Other solutions tackle disentanglement by encouraging a structure within the latent space of the VAE. FactorVAE [25] enforces independence by encouraging a factorial decomposition of the latent space. The Variationally Inferred Transformational Autoencoder (VITAE) proposes an architecture with two latent spaces to separate spatial transformation from visual style such as shape [15]. Likewise, the spatial VAE was designed to disentangle image orientation and translation from other latent variables [7], by introducing a geometric structure in the decoder. In contrast, our approach disentangles the variables by exploiting the specific geometric structure of the cryo-EM data set.

1.4. Contributions and Outline

We approach disentanglement of orientation and camera parameters by studying the geometric properties of the cryo-EM images projected in the latent space of a combination of a variational autoencoder and a generative adversarial network. We show that the projected images possess a structure of “orbits”, in the sense of Lie group theory. Such a structure is expected given the acquisition procedure of cryo-EM images. We use this observation to design an estimation method that computes the orientation and camera parameters of a given image, after outliers removal.

The paper is organized as follows. We begin by introducing, in Section 2, the elements of Lie group theory required for the analysis of the latent space. The methods for the neural network’s design, training, and latent space analysis are presented in Section 3. Section 4 introduces the simulated and experimental cryo-EM datasets that are used in the experiments. The results of our methods on these datasets are presented in Section 5.

2. Elements of geometry

2.1. Cryo-EM images and the action of rotations

We consider 2D images with compact domain $\Omega \subset \mathbb{R}^2$. We adopt the point of view of images as square-integrable functions x over the domain Ω ; i.e., we write $x \in L_2(\Omega)$, where $L_2(\Omega)$ is a Hilbert space. Cryo-EM images of a single particle, represented by a volume V in \mathbb{R}^3 , form a subspace of $L_2(\Omega)$. We first consider the ideal cryo-EM data space, written $\mathcal{C}_V(\Omega)$, which consists of hypothetical cryo-

EM images acquired without noise and with constant camera parameters. This space is defined as:

$$\begin{aligned} \mathcal{C}_V(\Omega) \\ = \{x \in L_2(\Omega) \mid \exists R_x \in SO(3), x = \text{PSF} * P(R_x \cdot V)\}, \end{aligned}$$

where $SO(3)$ is the group of 3D rotations, R_x is the rotation corresponding of the particle volume's orientation at acquisition time, P is a projection operator and PSF summarizes the camera parameters, as introduced in Section 1.2.1.

To understand the geometry of the space $\mathcal{C}_V(\Omega)$, we define the following action of the 3D rotations on cryo-EM images:

$$\begin{aligned} \rho : SO(3) \times \mathcal{C}_V(\Omega) &\rightarrow \mathcal{C}_V(\Omega), \\ (R, x) &\rightarrow R \cdot x = \text{PSF} * P(R \cdot R_x \cdot V). \end{aligned}$$

Mathematically, ρ is called a Lie group action of the Lie group $SO(3)$ on the space $\mathcal{C}_V(\Omega)$. We refer to [37, 1, 22] for details on Lie group actions.

Considering cryo-EM particles obtained from a single volume V with inplane rotations, we can define the subspace $\mathcal{C}_V^{2D}(\Omega)$ of $\mathcal{C}_V(\Omega)$ as:

$$\begin{aligned} \mathcal{C}_V^{2D}(\Omega) \\ = \{x \in L_2(\Omega) \mid \exists R_x \in SO(2), x = \text{PSF} * P(R_x \cdot V)\}, \end{aligned}$$

where the axis of the rotation in $SO(2)$ corresponds to the axis of the projection P . The action ρ of the subgroup $SO(2)$ on the subspace $\mathcal{C}_V^{2D}(\Omega)$ is a restriction to $\mathcal{C}_V^{2D}(\Omega)$ of the action ρ' of $SO(2)$ on 2D images, defined as follows:

$$\begin{aligned} \rho' : SO(2) \times L_2(\Omega) &\rightarrow L_2(\Omega), \\ (R, x) &\rightarrow R \cdot x = x \circ R^{-1}, \end{aligned}$$

where the image's domain is rotated by R^{-1} . From now on, we restrict our focus to the cryo-EM image subspace $\mathcal{C}_V^{2D}(\Omega)$ within the image space $L_2(\Omega)$ equipped with the action ρ' of 2D rotations.

Figure 1 represents the space of images $L_2(\Omega)$ as the toy Hilbert space \mathbb{R}^2 . It shows two cryo-EM images $x_1, x_2 \in \mathcal{C}_V^{2D}(\Omega)$ from the same particle V , and another image x_3 , as three points in this space. The action of $SO(3)$ is schematically represented there: the image x_1 is transformed into the image $x_2 = R \cdot x_1$ by the action of the rotation R .

2.2. Orbit and isotropy group

The orbit O_x of an image $x \in L_2(\Omega)$ by the action ρ' of $SO(2)$ is defined as the images reachable through the action of rotations on x : $O_x = \{x' \in L_2(\Omega) \mid \exists R \in SO(2), x' = R \cdot x\}$. On Figure 1, the orbit O_{x_1} of x_1 is represented as the green dotted circle. From the definition, O_{x_1} is also the orbit of x_2 and the two images x_1, x_2 are points on the green dotted circle.

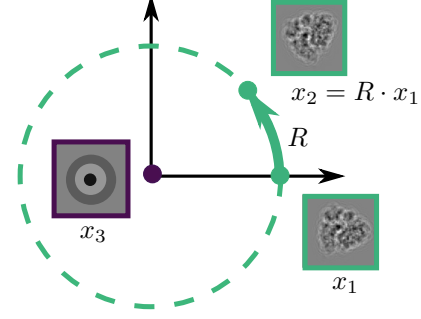


Figure 1. Action of 2D rotations on the space of images $L_2(\Omega)$, schematically represented as \mathbb{R}^2 .

The isotropy group G_x of a image x by the action ρ' is defined as the subgroup of $SO(2)$ formed by the rotations that leave x unchanged: $G_x = \{R \in SO(2) \mid R \cdot x = x\}$. G_x describes the intrinsic symmetry of the image x and the volume V : the more symmetric is x , the larger its isotropy group, where large is understood in the sense of inclusion.

The isotropy group of the images x_1, x_2 in Figure 1 is restricted to the identity \mathbb{I}_2 of the group $SO(2)$. Only the identity leaves the images x_1 and x_2 unchanged. In contrast, the isotropy group of the image x_3 is the whole Lie group of 2D rotations $SO(2)$. Any rotation leaves this image invariant. The image x_3 shows more symmetry than x_1 and x_2 , and thus has a larger isotropy group. The asymmetric details of x_1, x_2 are the sign of a smaller isotropy group.

As an intermediate example, consider an image exhibiting C_n symmetry, where C_n is the group of n -fold rotations corresponding to the set of 2D rotations with angles in $\frac{2\pi}{n}\mathbb{Z}/n\mathbb{Z}$. Such image has a greater isotropy group than x_1 and x_2 since $n - 1$ rotations leave it unchanged, on top of the identity \mathbb{I}_2 . But it exhibits a smaller isotropy group than x_3 since many rotations do affect it.

2.3. Ideal cryo-EM data space $\mathcal{C}_V^{2D}(\Omega)$

We describe the geometry of the ideal cryo-EM data space with in-plane rotations $\mathcal{C}_V^{2D}(\Omega)$, *i.e.* cryo-EM images acquired without noise and with constant camera parameters, using the orbit-stabilizer theorem. This theorem links the isotropy group (also called the stabilizer) and the orbit of an image.

Theorem 1 (Orbit-stabilizer Theorem) *Consider a Lie group G acting on a space H . Let $x \in H$ be an element of this space. Then, the orbit and isotropy group of x are related by: $O_x \sim G/G_x$ where \sim denotes an isomorphism and $/$ the quotient of groups.*

Theorem 1 states that an image with a large isotropy group - *i.e.* an image with a lot of symmetries - has a smaller orbit. On Figure 1, the images x_1, x_2 have a small isotropy

group and a circular orbit. In contrast, the image x_3 has a larger isotropy group and its orbit is a single point: x_3 itself.

Using the definition of the space $\mathcal{C}_V^{2D}(\Omega)$, we have the following result.

Proposition 1 *The space of cryo-EM images $\mathcal{C}_V^{2D}(\Omega)$ is isomorphic to $SO(2)/G_x$:*

$$\mathcal{C}_V^{2D}(\Omega) \sim SO(2)/G_x, \quad (4)$$

where G_x is the isotropy group of any image under the action ρ' .

The symmetries in the slice of volume V considered dictates the geometry of the space of the 2D cryo-EM images with inplane rotations.

2.4. Observed cryo-EM data space

We extend the discussion to the space of observed cryo-EM with in-plane rotations, *i.e.*, taking into account possible variations of the PSF and the noise model. The actual space of cryo-EM images is obtained by perturbing the space $\mathcal{C}_V^{2D}(\Omega)$ and can be interpreted as a ‘‘noisy’’ version of $\mathcal{C}_V^{2D}(\Omega)$, with a complex model of noise.

Locally at each cryo-EM image $x \in \mathcal{C}_V^{2D}(\Omega)$, the space of 2D images decomposes as a sum: $L_2(\Omega) = T_x \mathcal{C}_V^{2D}(\Omega) \oplus V_x$, where $T_x \mathcal{C}_V^{2D}(\Omega) = T_x O_x$ is the tangent space of the orbit O_x and V_x is a supplementary space. The space V_x represents the variations in images that do not correspond to 2D rotations, for example, the effects of camera parameters on the image intensity. Our objective is to learn a latent representation of the space of images where we can fit the space $\mathcal{C}_V^{2D}(\Omega)$ by fitting a spherical subspace to our projected data. Then, decomposing the latent space of images as $T_x \mathcal{C}_V^{2D}(\Omega) \oplus V_x$, we use the coordinate on $T_x \mathcal{C}_V^{2D}(\Omega)$ to describe the image’s orientation, and the coordinate on V_x to describe the other parameters.

3. Methods

3.1. VAE-GAN architecture and training

3.1.1 Review of VAE

We detail the combination of VAE [28, 39] and GAN [20] used in this paper. Consider a dataset $x_1, \dots, x_n \in \mathbb{R}^D$. A VAE models each data point x_i as the realization of a random variables X_i generated from a nonlinear probabilistic model with lower-dimensional unobserved latent variable Z_i taking value in \mathbb{R}^L , where $L < D$, such as:

$$X_i = f_\theta(Z_i) + \epsilon_i, \quad (5)$$

where ϵ_i represents *i.i.d.* measurement noise and follows a multivariate isotropic Gaussian: $\epsilon_i \sim N(0, \sigma^2 \mathbb{I}_D)$, and $Z_i \sim N(0, \mathbb{I}_L)$. The function f_θ belongs to a family \mathcal{F} of

nonlinear generative model parameterized by θ , and is typically represented by a neural network, called the decoder.

The VAE fits model (5) by training the decoder, while also training an encoder that simultaneously learns a distribution $q_\phi(z|x)$, within a variational family \mathcal{Q} parameterized by ϕ , of the posterior distribution of the latent variables Z_i . The VAE achieves its objective by minimizing an upper-bound of the negative log-likelihood, which writes as the sum of a reconstruction and regularization losses:

$$\begin{aligned} \mathcal{L}_{\text{VAE}} &= \mathcal{L}_{\text{rec}} + \mathcal{L}_{\text{reg}} \\ &= -\mathbb{E}_{q_\phi(z)} [\log p_\theta(x|z)] + \text{KL}(q_\phi(z|x) \parallel p(z)), \end{aligned}$$

where KL is the Kullback-Leibler divergence.

From a geometric perspective, VAE performs manifold learning as it learns θ to fit the manifold $f_\theta(\mathbb{R}^L)$ to the data. The function f_θ being continuous, VAEs can only learn manifolds homeomorphic to \mathbb{R}^L . As a consequence, a VAE needs a least two latent dimensions to capture a circle. For the simulated dataset with in-plane rotations, we choose $L = 3$ to capture a circle and an additional dimension of defocus. For the experimental dataset with in-plane rotations, we choose $L = 4$ to capture a circle, a dimension of defocus, and we add a dimension to capture other parameters like nuisance variables.

3.1.2 Review of GAN

We enhance the VAE by adding a GAN [9]. A GAN is a method to fit a model using an adversarial process. The GAN jointly fits the generative model to best capture the data distribution, and a discriminative model D that estimates the probability that a x_i came from the training data rather than the generative model.

The GAN achieves its objective by finding the binary classifier that gives the best discrimination between true and generated data and simultaneously encouraging the generator to fit the true data distribution. In practice, a GAN maximizes/minimizes the binary cross-entropy:

$$\mathcal{L}_{\text{GAN}} = \log p_{\text{Dis}}(x) + \log(1 - p_{\text{Dis}}(\text{Gen}(z)))$$

with respect to the discriminator or generator with x being a training sample.

From a geometric perspective, a GAN implicitly has to learn a complex similarity metric to discriminate actual data from generated data. For images, GAN usually produces reconstruction images of better visual quality. Learning an implicit metric is particularly interesting for cryo-EM images that are highly corrupted by noise.

3.1.3 VAE-GAN with geometric regularization

We add the GAN as a refinement to the reconstruction loss of the VAE. Our final architecture is shown on Figure 2. It

differs from [9] in two ways: (i) we keep the VAE’s reconstruction term, implemented with a binary cross-entropy, (ii) we do not use the L_2 norm on the discriminator features. Finally, we add a geometric regularizer to encourage the latent variables to form a cone: $\mathcal{L}_{\text{cone}} = (z_1^2 + z_2^2 - z_3^2)^2$, where z_1, z_2, z_3 are the first three dimensions of the latent space. Our loss writes:

$$\mathcal{L}_{\text{VAEGAN}} = \mathcal{L}_{\text{rec}} + \lambda_{\text{reg}} \mathcal{L}_{\text{reg}} + \lambda_{\text{GAN}} \mathcal{L}_{\text{GAN}} + \lambda_{\text{cone}} \mathcal{L}_{\text{cone}}$$

where $\lambda_{\text{reg}}, \lambda_{\text{GAN}}, \lambda_{\text{cone}}$ are hyperparameters.

The implementation of the encoder consists of convolutional layers with batch normalization [23] and a fully connected layer to predict the parameters of the variational distribution. The implementation of the decoder consists of convolutional layers, padding, and batch normalization. Details on the hyperparameters of the layers are provided in the supplementary materials.

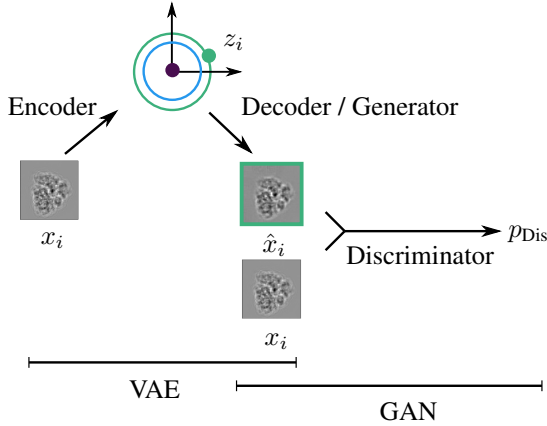


Figure 2. VAE-GAN architecture, illustrated with the simulated images. The encoder encodes the image x_i into a latent variable z_i , that is decoded into a reconstructed image \hat{x}_i by the decoder. The discriminator estimates the probability that x_i, \hat{x}_i are real images.

3.1.4 Model selection with hyper-parameter search

During training, the model is initialized with the standard heuristic [18]. For optimization, we use Adam [27] with standard parameters $\beta_1 = 0.9, \beta_2 = 0.999$. We use mini batches of size $B = 16$.

We tune the learning rate, the number of decoder’s layers, and the hyperparameters $\lambda_{\text{reg}}, \lambda_{\text{GAN}}$ with Bayesian optimization using the Hyperopt algorithm [8] and the Asynchronous Successive Halving Algorithm as scheduler [29] optimizing the validation loss. Details are provided in the supplementary materials. We do not tune hyperparameter λ_{cone} which is set to 1 as to represent our geometric constraint.

3.2. Exploratory Analysis and Estimations

After training of VAE-GAN, we project the cryo-EM dataset in the learned latent space. Section 2 established that the latent space decomposes, at a given cryo-EM image x , as $T_x O_x \oplus V_x$ where O_x is the orbit of x and V_x is a supplementary space. Taking V_x orthogonal to the orbit, we capture variations in the image that are rotationally invariant (e.g. defocus or other camera parameters). In this subsection, we curate and interpret the latent space in terms of those subspaces.

3.2.1 Outliers detection

We curate the dataset projected in the latent space by removing outliers. We expect most of the dataset to correspond to non-outliers images that come from the generative model of Equation 1 and share strong similarities. As such, the projections of these images are clustered together tightly in the latent space. In contrast, outliers are not drawn from the generative model and are likely to differ substantially. Their projections locate themselves at a distance from the non-outliers data.

We use and compare outlier detection methods for the data projected in the latent space: robust covariance (RobCov) method [19], isolation forest (IF) method [31] and local outlier factor (LOF) methods [24]. They all assign a measure m_i to each data point i , and a threshold m_{max} value that can be used to assign outlier status to a point when $m_i > m_{\text{max}}$. For RobCov, the measure m is the Mahalanobis distance centered at the origin of the latent space and with parameters given by the Hessian of the data. For IF, the data is represented as a tree through recursive partitioning, and the measure m is related to the path length averaged over a forest of random trees. For LOF, the measure m is related to the local density of the data around each data point.

We use the output of RELION to attribute the ground-truth label outlier/non-outlier to each datapoint [45]. Precisely, we consider the Z-score computed for each image in RELION, either at the 2D classification or 3D refinement steps, depending on the dataset considered, see Section 4. A data point is an outlier if its Z-score is larger than 2 in absolute value, it is a non-outlier otherwise. To assess the diagnostic ability of each outlier detection method, we measure the area under the curve (AUC) of the receiver operating characteristic (ROC) curve that is created by plotting the true positive rate (TPR) against the false positive rate (FPR) as m_{max} is varied for each method.

3.2.2 Estimation of defocus and orientation

We carry out principal component analysis (PCA) to identify the three dimensions bearing most of the variability:

$\mathbf{Z} = \mathbf{U}\Sigma\mathbf{V}^T$, where \mathbf{Z} is the design matrix of the data in the latent space. We call ‘‘reduced space’’ the space formed by the first two principal components of the PCA. The projection of the dataset in the reduced space is stored in the matrix $\mathbf{U}\Sigma$. We use the reduced coordinates $\mathbf{U} = (U_1, U_2)$ to yield defocus and orientation by converting them into polar coordinates:

$$(U_{1,i}, U_{2,i}) \rightarrow (r_i = \sqrt{U_{1,i}^2 + U_{2,i}^2}, \theta_i = \text{atan2} \frac{U_{2,i}}{U_{1,i}}). \quad (6)$$

We estimate the defocus of image i with the formula:

$$\widehat{\text{def}}_i = (q_3 - q_1) \frac{r_i - q_1(r)}{q_3(r) - q_1(r)} + q_1, \quad (7)$$

where $q_1(r), q_3(r)$ are the first and third quartiles of the empirical distribution of radii, and q_1, q_3 are the corresponding quartiles of the uniform distribution on the known range of defocuses [$0.5\mu\text{m}, 2.5\mu\text{m}$]. We estimate the orientation of image i as the angle θ_i given by the polar coordinates in the reduced space.

We evaluate the accuracy of this estimation procedure using the mean square error (MSE) between our predictions and the corresponding ground-truth, which is taken to be the defocus and orientation assigned by RELION. As we cannot expect to have the same origin of orientations nor the same orientation direction as RELION, we authorize a global shift Δ and a global change of sign when evaluating the MSE in orientations.

Furthermore, keeping in mind the cryo-EM downstream task that uses orientation estimates to reconstruct the 3D molecular shape, we allow the possibility of down-weighting each estimate, based on their assumed quality or precision. At reconstruction time, we can down-weight the associated images accordingly. We use the estimated defocus to build the weight as $w_i = e^{\widehat{\text{def}}_i} - 1$. The weight w_i reflects the level of confidence in the corresponding orientation estimate for image i : we are less confident in the orientation estimate corresponding to images with high defocus, *i.e.* blurry images.

Finally, the MSE formulas used to evaluate the accuracy of the defocus and orientation estimates write:

$$\text{MSE}_\theta = \text{argmin}_{\Delta, \pm} \left(\sum_i^n w_i (\pm\theta_i + \Delta - \theta_i^{(\text{true})})^2 \right) \quad (8)$$

$$\text{MSE}_{\text{def}} = \frac{1}{n} \sum_i^n (\widehat{\text{def}}_i - \text{def}_i^{(\text{true})})^2.$$

4. Datasets

4.1. Simulated dataset

We first created an ideal simulated dataset for which the simulation of micrographs was carried out using a transmis-

sion electron microscopy (TEM) simulator [41]. The TEM simulator simulates the process of cryo-EM images acquisition, see Section 1.1. We detail below the values of the parameters used required by the simulator. We used a single structural model of the human 80S ribosome [3]. We chose disks of diameter 1200 nm for the simulated grid holes, with an even ice thickness of 100 nm. We set the acceleration voltage of the simulated electron beam at 300 kV, with an energy spread of 1.3 V. We set the electron dose per image to 100 e/nm^2 .

In terms of image acquisition parameters, we set the magnification to 81000 with spherical and chromatic aberrations set at 2.7 mm. The aperture diameter was set at $50 \mu\text{m}$, the aperture angle at 0.1 mrad, and the focal length at 3.5 mm. The detector was defined as an array of 5760×4092 pixels, each of physical size $5 \mu\text{m}$, thus setting the pixel size in the images to 0.62 \AA . The simulation of noise was turned off, and the detector transfer function was assumed to be perfect. Micrographs were simulated assuming no motion of the particles, that were precisely placed in the field of view, while randomly rotated around the axis perpendicular to the grid plane (in-plane rotation). Micrographs were generated for each of the defocus values in the series going from 0.5 to $3.0 \mu\text{m}$ in steps of $0.5 \mu\text{m}$. Each micrograph contains 48 images of the ribosome particle, extracted with size 648×648 .

After this processing, we get a simulated dataset of $n = 2,544$ cryo-EM images that we downsample to size 128×128 . In this dataset, (i) there is one biomolecule’s shape: the chosen structural model of the human ribosome 80s, (ii), this molecule is rotated in a plane, (iii) the camera parameters are restricted to a set of 6 different defocuses by design, (iv) there is no noise. Images randomly sampled from this dataset are shown on the first line in Figure 3.

4.2. Experimental datasets

We added experimental datasets created from samples of human 80S ribosomes. These samples were prepared and imaged, yielding 7664 micrograph movies. We use RELION 3.0 [56] to process the micrographs. Preprocessing steps involved motion correction [53] and CTF estimation [40]. Particle picking was carried out using RELION’s ‘‘Autowpick’’ tool, yielding more than one million particles extracted as images rescaled to 180×180 with pixels of size 2.052 \AA .

The resulting set of images was subjected to three successive rounds of 2D classification in RELION, yielding a final dataset of 279,261 particles. We have extracted class 93 from the second round of 2D classification, as well as classes 30 and 39 from the third round. We compute the z-scores assigned to each image by running RELION’s ‘‘Particle sorting’’ tool on the respective 2D classification jobs: the z-score is a confidence score in the attribution of the given

	AUC	Angle (degr.)	Defocus (μm)
Sim.	N/A	1.72	0.18
Exp. (view 93)	0.79	37.38	0.44
Exp. (view 39)	0.86	18.61	0.45

Table 1. AUC and weighted rMSE for angle and defocus estimations, for the simulated dataset and the experimental datasets of views 93 and 39. AUC values are given for (isolation forest; $Z=2$).

2D class to the corresponding data point.

As a result of this processing, we have three experimental datasets of cryo-EM images, that we downsampled to size 128x128. In each of these datasets, (i) there is one biomolecule shape: the human 80S ribosome, (ii), this molecule is rotated in a plane. The first experimental in-plane dataset (view 39) represents the real dataset equivalent to the simulated case and has $n = 5,119$ images. The second (view 93) has $n = 8,278$ images. The third (view 30) has $n = 4,917$ images.

5. Results

5.1. Training VAE-GAN learns successive orbits

We train VAE-GAN on the simulated dataset and the three experimental datasets. Figure 3 shows the reconstructed images at different epochs during training, for the simulated dataset and the experimental dataset with view 93.

We observe that VAE-GAN successively learns the different Fourier components of the images. From a geometric perspective, VAE-GAN starts with a prior distribution on the latent variables that concentrates at the origin of the latent space, which represents the most symmetric image. During training, VAE-GAN expands this prior distribution to populate the different orbits of the action of the rotations. Starting from the origin of the latent space, it grows circles of increasing radii. Therefore, rotational symmetries successively disappear, as images find their place on their respective orbits.

At the end of the training, the images reconstructed from the simulated dataset are visually almost indistinguishable from the original images, see Figure 3. Each low-dimensional latent variable has captured the information specific to its image, while the decoder’s parameters have captured what is invariant across the images: the shape of the ribosome. The images reconstructed from the experimental dataset show a molecular shape that we recognize as the ribosome, see Figure 3. The VAE-GAN has performed denoising, an indication that we have captured the space $\mathcal{C}_V^{2D}(\Omega)$ introduced in Section 2.

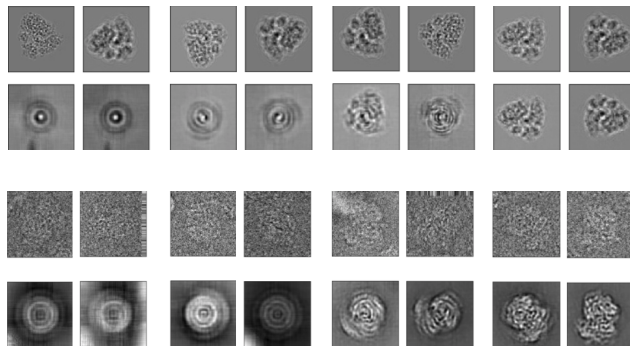


Figure 3. Reconstructions from simulated dataset (first two lines) and one experimental dataset (view 93, next two lines) during training, at four different epochs corresponding to the four columns.

5.2. Latent space of the simulated dataset

We perform an exploratory analysis in the latent space of the simulated dataset. Figure 4 shows the data projected on the first two components of the principal component analysis, colored by defocus and orientation’s angle. We observe that the latent space has learned the structure of orbits from the original space of images $L_2(\Omega)$, and has disentangled the camera parameter (defocus) from the ribosome’s orientation. In polar coordinates, the defocus is related to the radius, while the ribosome’s orientation is given by the angle, as shown in Figure 4. We had six values of defocuses in the simulated dataset, yet we observe that the last three have not been satisfactorily clustered. The defocus levels had made the corresponding images indeed not distinguishable at the resolution chosen after downsampling.

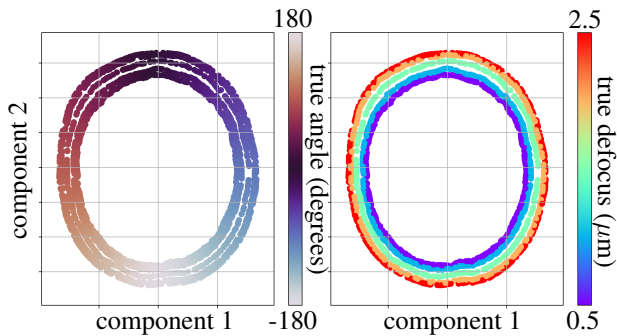


Figure 4. Cryo-EM images from the simulated dataset projected in the latent space. Left: colored by the angle of the in-plane rotation. Right: colored by defocus.

5.3. Latent space of inplane experimental datasets

We perform an exploratory analysis in the latent spaces of the experimental datasets with in-plane rotations.

5.3.1 Outlier detection

Figure 5 shows the data projected in the latent space of the experimental datasets with view 39, which is the view corresponding to the simulated dataset. We observe the same patterns as in the simulated case, with the addition of outliers that correspond to the corrupted images. The ROC curve of Figure 5 shows the results of the outliers detection methods, which efficiently reveal the outliers. For example, we report a AUC of 0.86 for the isolation forest method, see Table 1. The outlier detection methods perform equivalently well for the other experimental datasets, as shown in Table 1 and in the ROC curves in the supplementary materials.

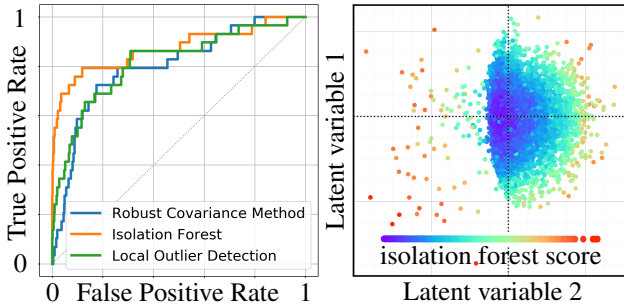


Figure 5. Left: ROC curve for outlier detections in the latent space. We use a threshold $z = 2$ from the “ground truth” given by the traditional computationally expensive methods. Right: Outlier detection in the latent space with isolation forests.

5.3.2 Orbits in the absence of symmetry

We perform an exploratory analysis in the latent space of the first two experimental datasets (views 39 and 93), for which the 2D projection of the ribosome shape has no apparent symmetry. The numerical results are presented in Table 1. We show the principal components of the latent space for view 39 in Figure 6 and refer the reader to the supplementary materials for the corresponding plots for view 93.

As the images in view 39 do not show any obvious symmetry, each orbit is isomorphic to S^1 as per Proposition 1. We observe a stratification of the latent space in concentric circles. As in the simulated case, the geometry of the group action leads to a natural disentanglement of the camera parameter (defocus) from the orientation’s angle, which can be extracted by polar coordinates, see Figure 6. Our method for estimating the defocus and orientation’s angle performs well with respective rMSEs of $0.58\mu\text{m}$ and 28.32 degrees, where the angle rMSE drops to 18.20 degrees (5% of relative error) when we perform the reweighting using the defocus’ estimation, see Table 1. We record similar rMSEs for the view 93, see Figure 8 (B). These results indicate that (unsupervised) estimation of defocus and orientations are possible using the latent space learned by VAE-GAN.

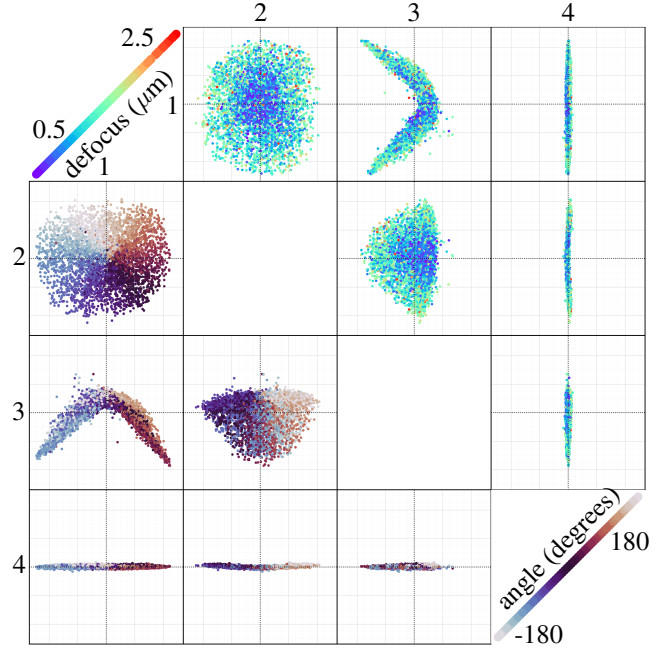


Figure 6. Cryo-EM images from the experimental dataset on view 39 in latent space ($L=4$).

5.3.3 Orbits in the presence of symmetry

We perform an exploratory analysis in the latent space of the third experimental datasets (view 30). In this dataset, the 2D projection of the ribosome’s shape exhibits symmetry, at the scale of the quality of the image reconstructions by the decoder, see Figure 7 (b). The symmetry can be described by the cycle group of 3-fold rotations, written C_3 , which consists of the set of 2D rotations of angles $0, 2\pi/3$, and $4\pi/3$. As a consequence, each orbit is isomorphic to S^1/C_3 as per Proposition 1.

We observe that the latent space has captured this geometry, which is revealed in Figure 8 (D, left) by the periodicity on the horizontal axis. A polar angle α in the latent space maps to α , or $\alpha + 2\pi/3$, or $\alpha + 4\pi/3$ in terms of the “true” angle. Additionally, we observe symmetry in reflection, corresponding to the symmetry on the vertical axis.

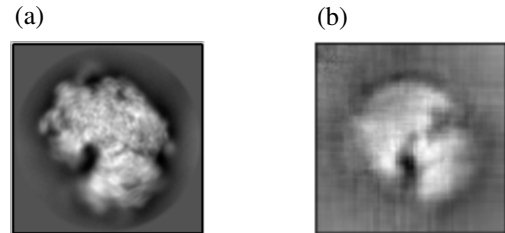


Figure 7. Symmetries of the particle in view 30. (a) 2D class average taken from RELION. (b) VAE-GAN reconstruction, suggesting a C_3 symmetry.

From a mathematical perspective, it is remarkable that VAE-GAN has captured the geometry of the orbit S^1/C_3 .

From a cryo-EM perspective, the downstream goal is the reconstruction of the unknown 3D shape of the biomolecule of interest. Structural biologists are not interested in symmetries caused by an insufficient resolution of the images reconstructed by the decoder. This case points out a potential failure mode, that can, however, be avoided, by ensuring an optimal resolution in the reconstructed images that avoid reconstructions' symmetries.

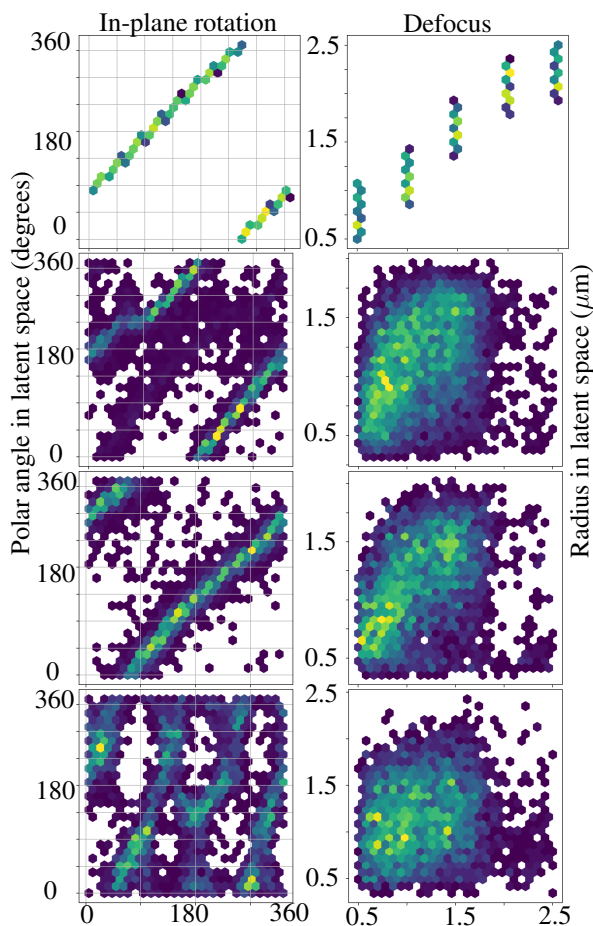


Figure 8. Unsupervised estimations. **(top)** Unsupervised estimation in the simulated dataset. Hexagonal bins with at least one data point are plotted. Highly populated bins are brighter. The rMSE is 1.72 degrees in the orientation angle and 0.18 μm in the defocus. **(bottom three)** Predicted angle versus angle from Relion (Views 93,39,30 going from top to bottom). Predicted defocus versus defocus from Relion.

6. Conclusion

We have combined variational autoencoders (VAEs) and generative adversarial networks (GANs) to learn the latent space of cryo-EM images. We recognize a geometric structure of stratification into orbits of the images by the action of the group of rotations. This analysis opens the door to

geometric approaches for unsupervised estimations of orientations and camera parameters, the two pillars of 3D reconstruction. This new avenue to cryo-EM biomolecular reconstruction would potentially unlock issues in scalabilities that traditional methods are starting to encounter in front of the fast-growing rate of data collection.

7. Acknowledgments

We thank Khanh Dao Duc and TJ Lane for very helpful comments on an earlier draft of the manuscript, and Daniel Ratner and Cornelius Gati for stimulating discussions and support throughout this work. F.P. acknowledges support from the National Institutes of Health (NIH), grant No. R35GM122543.

References

- [1] Dmitri Alekseevsky, Andreas Kriegl, Mark Losik, and Peter W Michor. The Riemannian Geometry of Orbit Spaces. The Metric, Geodesics, and Integrable Systems. *Publ. Math. Debrecen*, 62, 2003. 4
- [2] Joakim Andén and Amit Singer. Structural variability from noisy tomographic projections. *SIAM Journal on Imaging Sciences*, 2018. 2
- [3] Andreas M. Anger, Jean Paul Armache, Otto Berninghausen, Michael Habeck, Marion Subklewe, Daniel N. Wilson, and Roland Beckmann. Structures of the human and Drosophila 80S ribosome. *Nature*, 2013. 7
- [4] Todor Kirilov Avramov, Dan Vyenelo, Josue Gomez-Blanco, Swathi Adinarayanan, Javier Vargas, and Dong Si. Deep learning for validating and estimating resolution of cryo-electron microscopy density maps. *Molecules*, 2019. 3
- [5] Tamir Bendory, Alberto Bartesaghi, and Amit Singer. Single-particle cryo-electron microscopy: Mathematical theory, computational challenges, and opportunities. 8 2019. 3
- [6] Tristan Bepler, Andrew Morin, Alex J. Noble, Julia Brasch, Lawrence Shapiro, and Bonnie Berger. Positive-unlabeled convolutional neural networks for particle picking in cryo-electron micrographs. *Lecture Notes in Computer Science (including subseries Lecture Notes in Artificial Intelligence and Lecture Notes in Bioinformatics)*, 10812 LNBI:245–247, 2018. 3
- [7] Tristan Bepler, Ellen D. Zhong, Kotaro Kelley, Edward Brignole, and Bonnie Berger. Explicitly disentangling image content from translation and rotation with spatial-VAE. 9 2019. 3
- [8] James Bergstra and Yoshua Bengio. Random search for hyper-parameter optimization. *Journal of Machine Learning Research*, 13:281–305, 2012. 6
- [9] Anders Boesen, Lindbo Larsen, Sren Kaae Sønderby, Hugo Larochelle, Ole Winther, and Olwi@dtu Dk. Autoencoding beyond pixels using a learned similarity metric. Technical report, 2016. 5, 6
- [10] Leon Bottou. Large-scale machine learning with stochastic gradient descent. In *Proceedings of COMPSTAT 2010* -

- 19th International Conference on Computational Statistics, Keynote, Invited and Contributed Papers, 2010. 2
- [11] Ricky T. Q. Chen, Xuechen Li, Roger Grosse, and David Duvenaud. Isolating Sources of Disentanglement in Variational Autoencoders. (NeurIPS), 2018. 3
- [12] Xi Chen, Yan Duan, Rein Houthoofd, John Schulman, Ilya Sutskever, and Pieter Abbeel. InfoGAN: Interpretable representation learning by information maximizing generative adversarial nets. *Advances in Neural Information Processing Systems*, pages 2180–2188, 2016. 3
- [13] Yifan Cheng, Nikolaus Grigorieff, Pawel A. Penczek, and Thomas Walz. A primer to single-particle cryo-electron microscopy, 2015. 2
- [14] A. P. Dempster, N. M. Laird, and D. B. Rubin. Maximum Likelihood from Incomplete Data Via the EM Algorithm. *Journal of the Royal Statistical Society: Series B (Methodological)*, 1977. 3
- [15] Nicki Skafted Detlefsen and Sren Hauberg. Explicit Disentanglement of Appearance and Perspective in Generative Models. 6 2019. 3
- [16] Rafael Fernandez-Leiro and Sjors H.W. Scheres. A pipeline approach to single-particle processing in RELION. In *Acta Crystallographica Section D: Structural Biology*, volume 73, pages 496–502. International Union of Crystallography, 6 2017. 1
- [17] Joachim Frank. Two-Dimensional Averaging Techniques. In *Three-Dimensional Electron Microscopy of Macromolecular Assemblies*. 1996. 2
- [18] Xavier Glorot and Yoshua Bengio. Understanding the difficulty of training deep feedforward neural networks. In *Proc. of the Thirteenth International Conference on Artificial Intelligence and Statistics*, PMLR, pages 249–256, 2010. 6
- [19] Ramanathan Gnanadesikan and Jon R. Kettenring. Robust Estimates, Residuals, and Outlier Detection with Multiresponse Data. *Biometrics*, 28(1):81–124, 2014. 6
- [20] Ian J. Goodfellow, Jean Pouget-Abadie, Mehdi Mirza, Bing Xu, David Warde-Farley, Sherjil Ozair, Aaron Courville, and Yoshua Bengio. Generative Adversarial Nets. Technical report, 2014. 5
- [21] Timothy Grant, Alexis Rohou, and Nikolaus Grigorieff. Cistem, user-friendly software for single-particle image processing. *eLife*, 2018. 2
- [22] Stephan Huckemann, Thomas Hotz, and Axel Munk. Intrinsic shape analysis: Geodesic PCA for riemannian manifolds modulo isometric lie group actions. *Statistica Sinica*, 20(1):1–58, 2010. 4
- [23] Sergey Ioffe and Christian Szegedy. Batch Normalization: Accelerating Deep Network Training by Reducing Internal Covariate Shift. 2015. 6
- [24] Ramin Jahanbegloo and Ramin Jahanbegloo. Identifying Density-Based Local Outliers. (October 2017):1–22, 2012. 6
- [25] Hyunjik Kim and Andriy Mnih. Disentangling by factorising. *35th International Conference on Machine Learning, ICML 2018*, 6:4153–4171, 2018. 3
- [26] Dari Kimanius, Bjrn O. Forsberg, Sjors H.W. Scheres, and Erik Lindahl. Accelerated cryo-EM structure determination with parallelisation using GPUS in RELION-2. *eLife*, 2016. 3
- [27] Diederik P. Kingma and Jimmy Lei Ba. Adam: A Method for Stochastic Optimization. In *Proc of the 3rd International Conference for Learning Representations*, 2015. 6
- [28] Diederik P. Kingma and Max Welling. Auto-Encoding Variational Bayes. In *Proceedings of the 2nd International Conference on Learning Representations (ICLR)*, 2014. 5
- [29] Liam Li, Kevin Jamieson, Afshin Rostamizadeh, Ekaterina Gonina, Moritz Hardt, Benjamin Recht, and Ameet Talwalkar. Massively Parallel Hyperparameter Tuning. pages 1–16, 2018. 6
- [30] Xueming Li, Paul Mooney, Shawn Zheng, Christopher R. Booth, Michael B. Braunfeld, Sander Gubbens, David A. Agard, and Yifan Cheng. Electron counting and beam-induced motion correction enable near-atomic-resolution single-particle cryo-EM. *Nature Methods*, 2013. 1
- [31] Fei Tony Liu, Kai Ming Ting, and Zhi-Hua Zhou. IsolationForest: Isolation Forest. *2008 Eighth IEEE International Conference on Data Mining*, 2008. 6
- [32] Romain Lopez, Jeffrey Regier, Michael I. Jordan, and Nir Yosef. Information constraints on auto-encoding variational Bayes. *Advances in Neural Information Processing Systems*, 2018-Decem(1):6114–6125, 2018. 3
- [33] Christos Louizos, Kevin Swersky, Yujia Li, Max Welling, and Richard Zemel. The Variational Fair Autoencoder. pages 1–11, 2015. 3
- [34] Vladan Lučić, Alexander Rigort, and Wolfgang Baumeister. Cryo-electron tomography: The challenge of doing structural biology in situ, 2013. 2
- [35] G. McMullan, A. R. Faruqi, and R. Henderson. Direct Electron Detectors. In *Methods in Enzymology*. 2016. 1
- [36] Eva Nogales. The development of cryo-EM into a mainstream structural biology technique. *Nature Methods*, 2015. 1
- [37] Mikhail Postnikov. *Riemannian Geometry*. Encyclopaedia of Mathem. Sciences. Springer, 2001. 4
- [38] Ali Punjani, John L. Rubinstein, David J. Fleet, and Marcus A. Brubaker. CryoSPARC: Algorithms for rapid unsupervised cryo-EM structure determination. *Nature Methods*, 2017. 2, 3
- [39] Danilo J. Rezende, Shakir Mohamed, and Daan Wierstra. Stochastic Backpropagation and Approximate Inference in Deep Generative Models. In *Proceedings of the 31st International Conference on Machine Learning*, 2014. 5
- [40] Alexis Rohou and Nikolaus Grigorieff. CTFFIND4: Fast and accurate defocus estimation from electron micrographs. *Journal of Structural Biology*, 2015. 2, 7
- [41] Hans Rullgård, L.-G. Öfverstedt, Sergey Masich, Bertil Danesholt, and Ozan Öktem. Simulation of transmission electron microscope images of biological specimens. *Journal of Microscopy*, 2011. 7
- [42] Ruben Sanchez-Garcia, Joan Segura, David Maluenda, Jose Maria Carazo, and Carlos Oscar S. Sorzano. Deep Consensus, a deep learning-based approach for particle pruning in cryo-electron microscopy. *IUCrJ*, 5:854–865, 2018. 3

- [43] Sjors H.W. Scheres. A bayesian view on cryo-EM structure determination. *Journal of Molecular Biology*, 2012. [2](#), [3](#)
- [44] Sjors H.W. Scheres. RELION: Implementation of a Bayesian approach to cryo-EM structure determination. *Journal of Structural Biology*, 2012. [2](#)
- [45] Sjors H.W. Scheres. Semi-automated selection of cryo-EM particles in RELION-1.3. *Journal of Structural Biology*, 2015. [2](#), [6](#)
- [46] Fred J. Sigworth. A maximum-likelihood approach to single-particle image refinement. *Journal of Structural Biology*, 1998. [2](#)
- [47] Fred J. Sigworth. Principles of cryo-EM single-particle image processing, 2016. [2](#)
- [48] Ganesh Thiagarajan and George Z. Voyiadjis. β -VAE: Learning basic visual concepts with a constrained variational framework. *Proc. of ICLR*, pages 1–13, 2017. [3](#)
- [49] Rebecca F. Thompson, Matthew G. Iadanza, Emma L. Hesketh, Shaun Rawson, and Neil A. Ranson. Collection, pre-processing and on-the-fly analysis of data for high-resolution, single-particle cryo-electron microscopy. *Nature Protocols*, 2019. [1](#)
- [50] Thorsten Wagner, Felipe Merino, Markus Stabrin, Toshio Moriya, Claudia Antoni, Amir Apelbaum, Philine Hagel, Oleg Sitsel, Tobias Raisch, Daniel Prumbaum, Dennis Quentin, Daniel Roderer, Sebastian Tacke, Birte Siebolds, Evelyn Schubert, Tanvir R. Shaikh, Pascal Lill, Christos Gatsogiannis, and Stefan Raunser. SPHIRE-crYOLO is a fast and accurate fully automated particle picker for cryo-EM. *Communications Biology*, 2(1):1–13, 2019. [3](#)
- [51] Feng Wang, Huichao Gong, Gaochao Liu, Meijing Li, Chuangye Yan, Tian Xia, Xueming Li, and Jianyang Zeng. DeepPicker: A deep learning approach for fully automated particle picking in cryo-EM. *Journal of Structural Biology*, 195(3):325–336, 2016. [3](#)
- [52] Kai Zhang. Gctf: Real-time CTF determination and correction. *Journal of Structural Biology*, 2016. [2](#)
- [53] Shawn Q. Zheng, Eugene Palovcak, Jean Paul Armache, Kliment A. Verba, Yifan Cheng, and David A. Agard. MotionCor2: Anisotropic correction of beam-induced motion for improved cryo-electron microscopy, 2017. [1](#), [7](#)
- [54] Ellen D. Zhong, Tristan Bepler, Joseph H. Davis, and Bonnie Berger. Reconstructing continuously heterogeneous structures from single particle cryo-EM with deep generative models. pages 1–16, 2019. [3](#)
- [55] Yanan Zhu, Qi Ouyang, and Youdong Mao. A deep convolutional neural network approach to single-particle recognition in cryo-electron microscopy. *BMC Bioinformatics*, 18(1):1–10, 2017. [3](#)
- [56] Jasenko Zivanov, Takanori Nakane, Björn O. Forsberg, Dari Kimanius, Wim J.H. Hagen, Erik Lindahl, and Sjors H.W. Scheres. New tools for automated high-resolution cryo-EM structure determination in RELION-3. *eLife*, 2018. [2](#), [7](#)